nature nanotechnology

Article

https://doi.org/10.1038/s41565-023-01410-6

Tunable phononic coupling in excitonic quantum emitters

Received: 15 July 2022

Accepted: 28 April 2023

Published online: 01 June 2023

Check for updates

Adina Ripin[1], Ruoming Peng[2] ✉, Xiaowei Zhang[3], Srivatsa Chakravarthi[1], Minhao He[1], Xiaodong Xu[1,3], Kai-Mei Fu[1,2,4], Ting Cao[3] & Mo Li[1,2] ✉

Engineering the coupling between fundamental quantum excitations is at the heart of quantum science and technologies. An outstanding case is the creation of quantum light sources in which coupling between single photons and phonons can be controlled and harnessed to enable quantum information transduction. Here we report the deterministic creation of quantum emitters featuring highly tunable coupling between excitons and phonons. The quantum emitters are formed in strain-induced quantum dots created in homobilayer WSe_2. The colocalization of quantum-confined interlayer excitons and terahertz interlayer breathing-mode phonons, which directly modulates the exciton energy, leads to a uniquely strong phonon coupling to single-photon emission, with a Huang–Rhys factor reaching up to 6.3. The single-photon spectrum of interlayer exciton emission features a single-photon purity >83% and multiple phonon replicas, each heralding the creation of a phonon Fock state in the quantum emitter. Due to the vertical dipole moment of the interlayer exciton, the phonon–photon interaction is electrically tunable to be higher than the exciton and phonon decoherence rate, and hence promises to reach the strong-coupling regime. Our result demonstrates a solid-state quantum excitonic–optomechanical system at the atomic interface of the WSe_2 bilayer that emits flying photonic qubits coupled with stationary phonons, which could be exploited for quantum transduction and interconnection.

The quantized vibrational motion in solid-state quantum systems, that is, phonons, has been exploited as an important modality that interfaces with electrons and photons for quantum information science and applications[1]. In bulk diamond, optical phonons with a frequency of 40 THz have been mapped to Raman scattered photons to realize non-local entanglement at room temperature[2–4]. In microscopic cavity optomechanical systems, phonons of megahertz to gigahertz frequencies have been used to store and transfer quantum states between microwave and optical photons[5,6]. In molecular quantum emitters (QEs), coupling with the phonons of the host medium is generally considered detrimental to the quantum properties[7], although the molecule's internal optomechanical degree of freedom has been exploited[8]. These archetypical demonstrations utilize either bulk phonon modes involving collective vibration of many atoms or a phonon band including a large number of unresolved modes, resulting in a relatively low phonon–photon scattering probability or coupling rate. To further explore the phonon degree of freedom in the quantum regime, therefore, it is highly desirable to engineer new quantum light sources that afford strong phonon–photon coupling involving a well-defined single-phonon mode, preferably with an intermediate high frequency and tunable coupling strength.

[1]Department of Physics, University of Washington, Seattle, WA, USA. [2]Department of Electrical and Computer Engineering, University of Washington, Seattle, WA, USA. [3]Department of Materials Science and Engineering, University of Washington, Seattle, WA, USA. [4]Physical Sciences Division, Pacific Northwest National Laboratory, Richland, WA, USA. ✉e-mail: pruoming@uw.edu; moli96@uw.edu

https://doi.org/10.1038/s41565-023-01410-6

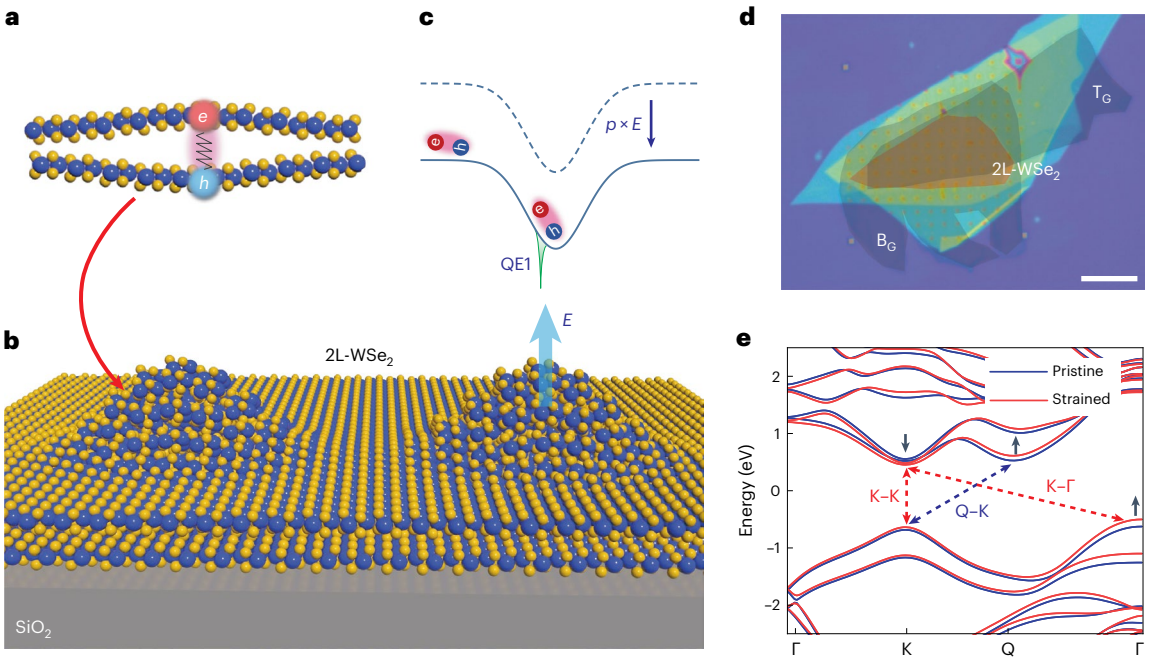

Fig. 1 | Strain-engineered 2D QEs. a, Schematic of the interlayer BM phonon which couples strongly with IXs in bilayer (2L) WSe_2 because the IX with vertical dipole moments is directly modulated by the vibrational mode. **b**, Illustration of bilayer WSe_2 transferred onto SiO_2 nanopillars, forming quantum dots with local strain modulation, which host the QEs. **c**, Strain-induced potential traps with natural defects (green dips), where excitons are funnelled into and localized. The QE energy can be efficiently tuned by electric fields through the Stark effect. **d**, Optical microscopy image of a representative device. The bilayer WSe_2, encapsulated by hBN and gated with top and bottom graphite layers (T_G, B_G), is transferred onto an array of SiO_2 nanopillars. Metal electrodes are subsequently deposited to contact the graphite layers. Scale bar, 10 µm. **e**. The DFT-calculated band structure of the bilayer WSe_2 in pristine (blue) and under 1% tensile strain (red) conditions. Without strain, phonon-assisted indirect bandgap transition Q–K can occur. A sufficient amount of strain can shift the conduction band minimum from the Q point to the K point and shift the valance band Γ point up such that direct K–K and indirect K–Γ transitions can become favourable.

QEs in two-dimensional materials[9], including transition metal dichalcogenide (TMD), hexagonal boron nitride (hBN) and their heterostructures, provide new opportunities for engineering quantum-regime phonon–photon coupling. These atomically thin materials have bright exciton emissions and are very rich in optically (Raman) active phonon modes[10,11]. Their multilayers further afford intralayer and interlayer phonons with a vast span of frequencies from optical to acoustic ranges. Moreover, QEs in 2D materials can be deterministically created with several approaches, such as strain engineering and ion implantation[12–14]. These techniques have enabled the site-controlled creation of QEs with a high yield and high single-photon purities. Because they are hosted in atomically thin materials, 2D QEs are amenable to photonic integration to facilitate photon extraction[15] and Purcell effect enhancement of emission[16], providing a versatile quantum system to explore phonon–photon interactions.

Here we report strong and tunable phonon–photon coupling in strain-engineered 2D QEs that are deterministically created in bilayer WSe_2. These 2D QEs emit single photons with high purity and have a high electrical tunability in emission energy. Remarkably, in the single-photon emission spectra, multiple well-resolved phonon replica lines are observed, each of which heralds the creation of a phonon Fock state. The large phonon–photon coupling in this QE system stems from the colocalization and quantum confinement of the interlayer excitons (IXs) and the breathing-mode (BM) phonons, which directly modulates the exciton energy. The very high phonon–photon coupling strength is characterized by a large and electrically tunable Huang–Rhys factor that is, to the best of our knowledge, the highest achieved in solid-state QE systems[17–20]. The demonstrated strong and tunable single phonon–photon coupling provides an invaluable resource for engineering quantum light emission systems with an internal mechanical degree of freedom for quantum information processing.

Strain engineering of single-photon emitters in bilayer WSe_2

The bilayer WSe_2 is an ideal system to explore the phonon–photon interaction because it affords many Raman-active phonon modes covering a broad frequency range[21,22]. Particularly, as shown in Fig. 1a, the interlayer BM phonon strongly couples with the IXs because the vertical dipole moment of an IX is modulated directly by the interlayer vibration. To explore this coupling at the single-photon level, we use a strain-engineering approach to create QEs in bilayer WSe_2 by transferring them onto patterned nanopillars[12–14], as illustrated in Fig. 1a. The nanopillars induce local strain that modulates the bandgap and thus creates spatial confinement of IXs in the bilayer WSe_2 (ref. 23), resulting in quantum dots that host QEs[24]. Figure 1c illustrates the potential traps formed by the localized strain in the bilayer WSe_2. The optically excited IXs are funnelled into the traps where they are bound with natural defects and recombine to emit single photons. In comparison with excitons in monolayer TMDs, IXs in bilayer WSe_2 have a large out-of-plane electric dipole moment[22,25–27]. Therefore, they couple efficiently to both a perpendicular electric field that generates a Stark shift and interlayer vibration. Stark shifts of the IX energy by more than 50 meV have been achieved in bilayer WSe_2 and other TMDs[28,29]. Multiple QEs can be created at each site in the nanopillar array (Fig. 1b). Although the QEs at different sites have different emission energies due to the variation of the local parameters such as the amount of strain and the energy level of the defects, applying a local electric field to each of them using separate gate electrodes can tune their emission energies to be the same.

Figure 1d shows an optical image of a fabricated device. A stack of bilayer WSe_2 encapsulated by two hBN layers (~30 nm), with top and bottom graphite electrodes, is transferred onto a substrate with an array of nanopillars made of SiO_2. The top and bottom graphite electrodes

https://doi.org/10.1038/s41565-023-01410-6

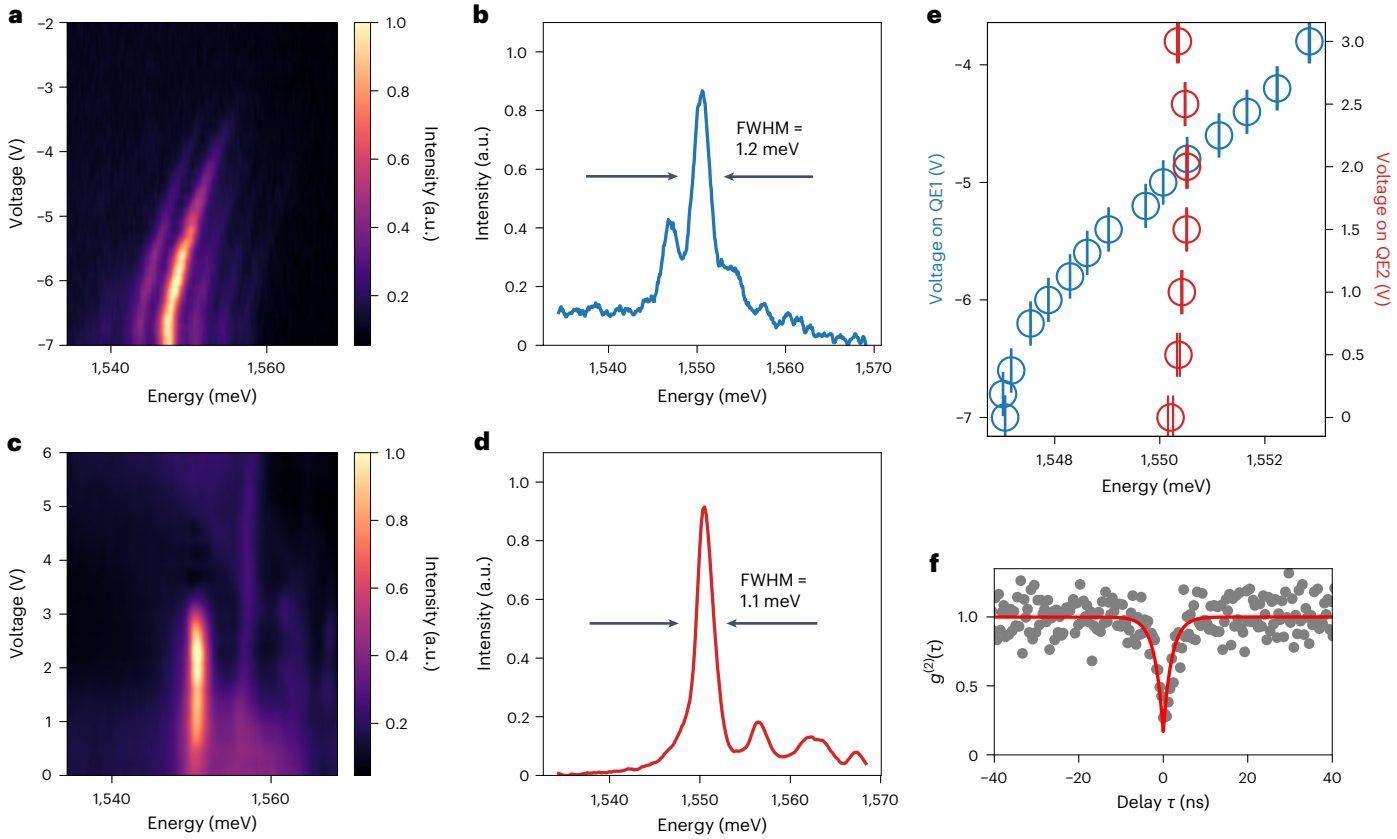

Fig. 2 | Tunable 2D QEs. a, PL spectra of QE1 as a function of the gate voltage. The emitter turns on at around −4 V and is accompanied by sidebands that are turned on at the same voltage. **b**, Line-cut of the PL in **a** at $V_g = -5$ V, showing an FWHM linewidth of 1.2 meV. **c**, PL spectra of QE2 as a function of the gate voltage. The emitter is on at zero gate bias, suggesting it has a different origin to that of QE1. At around 3.5 V, the emitter is turned off. **d**, Line-cut of the PL in **c** at $V_g = 2$ V, showing an FWHM linewidth of 1.1 meV. **e**, Modulation of emitter energy of QE1 and QE2 with gate voltage. The two QEs can be tuned to have nearly identical energy and linewidth. The centre energy of the QE is extracted through a least-squares fit to a Lorentzian function of the PL spectra. The error bars represent the standard error in this fit for $n = 190$ PL points. **f**, Second-order photon correlation $g^{(2)}(\tau)$ measured from a representative QE, showing antibunching with $g^{(2)}(0) = 0.169 \pm 0.005$, indicating a single-photon purity of 83%. The data is shown in grey, and the fit to the data (as detailed in Supplementary Note 1) is shown in red.

enable electrical tuning of the QEs' energy. Figure 1e shows the density functional theory (DFT)-calculated band structure of bilayer WSe_2 in its pristine state and strained state with 1% tensile strain. In pristine bilayer WSe_2, indirect bandgap transition Q–K can occur, assisted by various single-phonon or two-phonon processes[22]. When under a sufficient amount of strain, the conduction band minimum is shifted from the Q point to the K point, and the valance band Γ point is shifted up such that direct K–K and indirect K–Γ transitions can become favourable in energy, enabling strong exciton coupling to zero-momentum phonons[22,30–33]. Therefore, depending on the level of local strain, IX species corresponding to either Q–K, K–Γ or K–K transitions can dominate the photon emission. These IX species have different dipole moments[27], but because their energy is susceptible to the interlayer separation, they all couple to BM phonon strongly.

Tunable QEs

We fabricated multiple samples. In each sample, we can find multiple QEs at different nanopillars in the array. All the measurements were performed in a cryostat at a temperature of 10 K. Figure 2a shows the photoluminescence (PL) spectrum of a QE (QE1) as a function of top-gate voltage (with the bottom-gate grounded). The excitation laser is 632.8 nm with a fixed power of 15 μW. QE1 remains dark until the gate voltage reaches a negative value of ~−3.5 V, after which a bright, sharp PL peak is observed at 1,555 meV with a full-width at half-maximum (FWHM) linewidth of 1.1 meV. This turn-on behaviour may be attributed to the IXs being bound to a donor (or acceptor)-type defect, meaning that electron (or hole) doping is needed for IX to bind to the defect and form a QE. Both donor- and acceptor-type defects in WSe_2 have been reported previously[34]. Among the 19 IX QEs in five devices (Supplementary Fig. 1) we have measured, 16 of them turn on at negative gate voltage, and three of them turn on at positive gate voltage. The gate voltage induces doping because of the top/bottom structure asymmetry of the devices, including the nanopillars at the bottom, and the thicker bottom hBN layer that prevents piercing by the nanopillars. There is also possible non-negligible current leakage through the layers. After QE1 is turned on, its emission can be redshifted by more than 6.4 meV (~3.3 nm in wavelength) with the application of gate voltage up to −7 V. From the dipole model of field tunability, $\Delta U = p \times E$, we calculate the IX dipole moment of QE1 p to be 0.341 e·nm, consistent with previous experimental results for K–Γ IX (ref. 22,25,26). Among the 19 IX QEs we have measured (Supplementary Table 1), we observed three ranges of dipole moments around 0.32, 0.46 and 0.63 e·nm. Respectively, they correspond to the theoretical values of K–Γ, Q–K and K–K IXs. As shown by the DFT-calculated band structure under strain (Fig. 1d) and previously reported experimental results, which type of IX dominates the QE depends on the local strain level[22,27,30,35–38]. Because the local strain level can vary considerably at each nanopillar, and QE formation results from the accidental occurrence of a suitable defect, the strain levels at different QEs can be very different, thereby leading to different types of IX. Even higher tunability can be achieved with QEs in heterobilayers, such as moiré excitons[39], which have an even larger dipole moment. Figure 2c shows the PL spectra of another QE (QE2),

https://doi.org/10.1038/s41565-023-01410-6

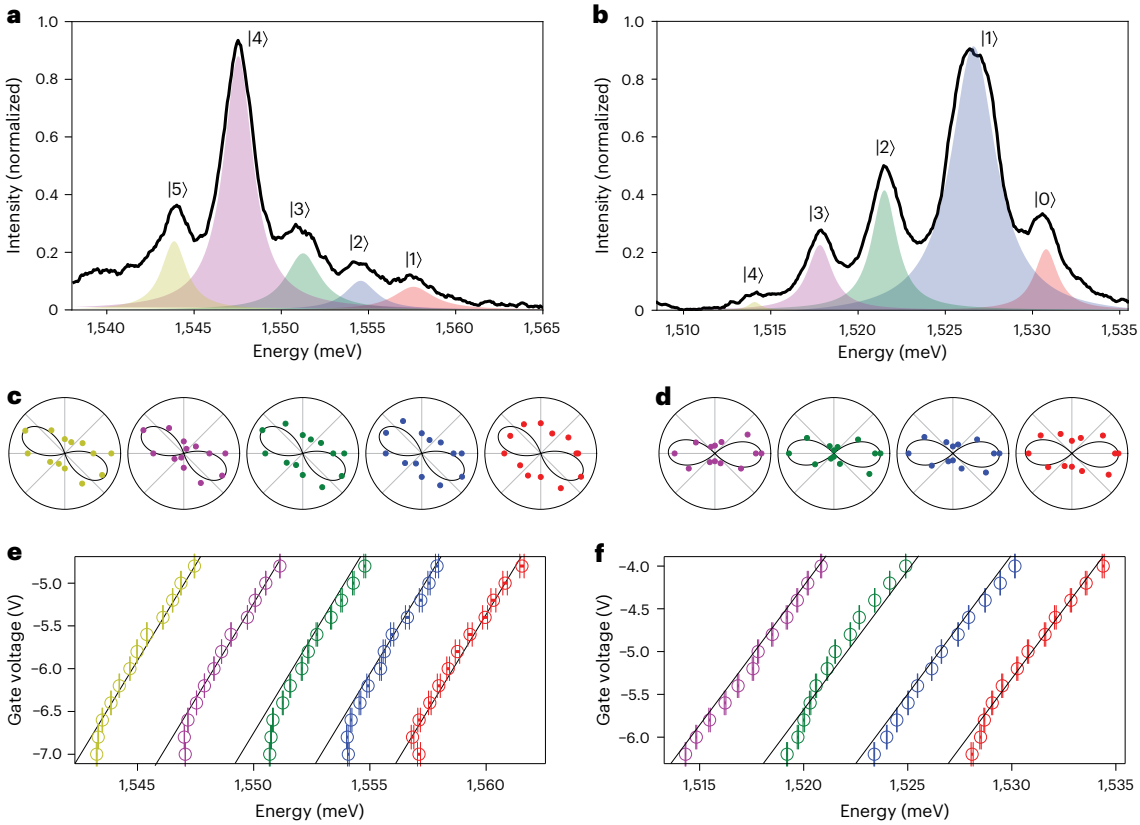

Fig. 3 | Single-phonon emission lines. a, PL spectrum of QE1 at −6.4 V. Five emission lines can be observed and are fitted with Lorentzian functions (shaded area). **b**, PL spectrum of QE3 at −5.0 V. Four emission lines can be observed and are fitted with Lorentzian functions (shaded area). **c**,**d**, The photons from the sidebands of QE1 (**c**) and QE3 (**d**) are polarized with the same orientation. The thin black lines are guides for linear polarization. **e**,**f**, The sideband energy of QE1 (**e**) and QE3 (**f**) is tuned by the gate voltage synchronously at the same rate with an unchanged spacing in energy. The centre energy of each QE sideband is extracted through a least-squares fit to a Lorentzian function of the PL spectra. The error bars represent the standard error in this fit for $n = 400$ PL points.

which behaves differently from IX QEs. QE2 is bright at zero gate voltage with an emission energy of 1,550 meV, which remains unchanged with varying gate voltage until 3.0 V when the emission is turned off. This type of QE can be attributed to defect-bound intralayer excitons, which do not couple to the out-of-plane electric field and are rarer (only three out of 22 QEs we measured). However, a sufficiently high electric field can cause electron or hole tunnelling to another layer of WSe_2, consequently turning off the intralayer exciton emission.

The different responses of the two types of QEs to electrical modulation allow us to tune them to the same energy, as summarized in Fig. 2e. In Fig. 2b,d, when gate voltages of −5.0 V and 2.0 V are applied to QE1 and QE2, respectively, both QEs emit photons at 1,550 meV with similar linewidths. Figure 2f shows the second-order photon correlation $g^{(2)}(\tau)$ measured from a device (QE13 in Supplementary Fig. 1) behaving similarly to QE1. A filter with ~5.0 nm (9.7 meV) bandwidth was used to select the measurement range. The result shows clear antibunching with $g^{(2)}(0) = 0.169 \pm 0.005$, indicating a single-photon purity of 83%. From fitting the autocorrelation data, we estimate the QE lifetime to be 2.0 ± 0.25 ns. We have measured similar antibunching results from many QEs with linewidths in the range of 1–3 meV across different devices (Supplementary Fig. 3). The demonstrated wide electrical tuning range makes these 2D QEs promising for achieving scalable arrays of indistinguishable single-photon sources. In areas without nanopillars, we measure IX emission with a much broader linewidth > 5 meV and without antibunching, which is consistent with previous reports[22,25,27,40]. In addition, we observed no pronounced emission in a wide energy range below the bandgap (Supplementary Fig. 13), and therefore emission due to in-gap defect states can be ruled out. Therefore, we conclude that the combination of defect and strain engineering is necessary to create the QEs[13]. There are several possible types of defects in WSe_2, including selenium vacancies, tungsten antisites, oxygen-passivated selenium vacancies and oxygen interstitials[24,41–44]. Although it is unclear which type of defect is responsible for forming the QE—microscopy studies are needed to reveal this—the selenium vacancy has a higher density than other types and hence is more likely to occur at the nanopillars.

Single exciton–phonon coupling

A very notable feature in the PL spectra of QE1 (Fig. 2a) is multiple emission lines on both sides of the main peak. These emission lines are turned on/off by the gate voltage along with the main peak and modulated at the same rate, suggesting their correlation. We observed similar features in many devices. Figure 3a,b shows the PL spectra of QE1 and another QE (QE3), measured with gate voltages of −6.4 and −5.0 V, respectively. Five emission lines can be observed with spacings in the range of 3.0–3.7 meV for QE1 (Fig. 3a) and 3.7–5.1 meV for QE3 (Fig. 3b). We then measured the polarization of the photons from each emission line. As shown in Fig. 3c,d, photons from each QE's emission line are linearly polarized with the same orientation. Figure 3e,f shows that the energies of these lines are tuned by the gate voltage synchronously at the same rate, with their spacings unchanged. All these features allow us to conclude that these emission lines originate from the same QE, rather than other emitters nearby.

The observation of multiple well-resolved emission lines can be explained as phonon replicas due to the coupling between a single IX and a single-phonon mode that are colocalized in the QE. Their coupling

https://doi.org/10.1038/s41565-023-01410-6

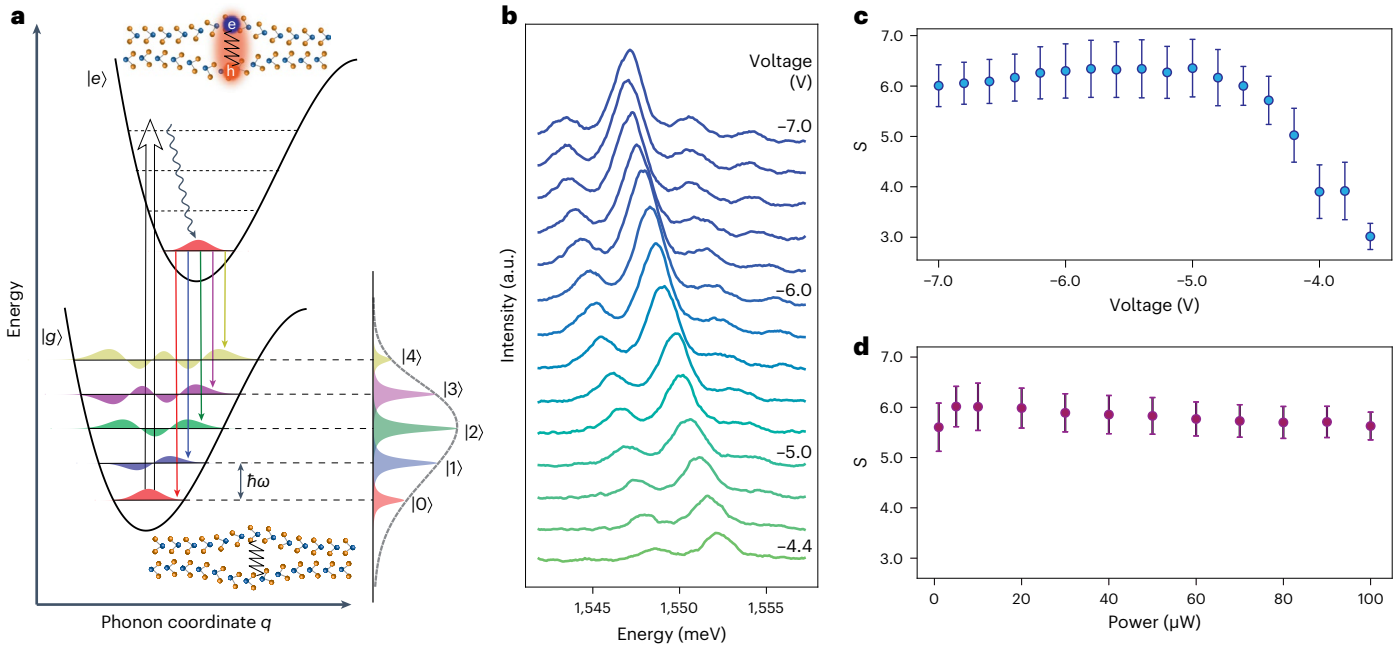

Fig. 4 | Strong and tunable single phonon–exciton coupling. a. A diagram of the Franck–Condon model of exciton–phonon coupling in a 2D QE. The lower parabolic potential represents the ground-state PES of the QE. Multiple phonon states with an energy spacing of 3.4 meV are shown, with their wavefunctions illustrated. The upper potential represents the excited-state PES of the QE with optically pumped IX. The phonon mode that strongly couples with the IX is the BM, in which the layers of WSe_2 move in opposite directions, modulating the interlayer spacing and IX energy. Based on the Huang–Rhys theory, the phonon line intensity should have a Poisson distribution with an average phonon number at *S*, which is the Huang–Rhys factor. The anharmonic effect can result in unequal energy spacing for the adjacent phonon lines. **b**, PL spectra of QE1 at different gate voltages. The intensity distribution of the phonon lines is strongly modulated by the gate voltage. We extract the value of *S* by fitting the intensity with the Poisson distribution. **c**, *S* as a function of the gate voltage. *S* initially increases with the voltage, in agreement with theory, and levels off after −5.0 V. **d**, *S* as a function of pump power. The error bars in **c** and **d** represent the standard error in the least-squares fit to the Poisson distribution for $n = 450$. More details of this calculation can be seen in Supplementary Note 8.

can be understood with the Franck–Condon principle, as illustrated in Fig. 4a (ref. 19,20,45,46). The ground state of the QE and its excited state when an IX is generated can be modelled with two potential energy surfaces (PESs). Each PES is populated with phonon states that are not evenly spaced because of the anharmonicity of the PES. Under the linear coupling approximation, the phonon–exciton coupling is represented by a shifted equilibrium position of the excited-state PES relative to the ground state. At low temperatures, the QE at the ground-state PES has nearly zero phonon occupancy. When an exciton is created by the pump laser, the QE is excited into a higher-energy PES and quickly relaxes to its zero phonon level. Upon exciton recombination, the QE emits a single photon and relaxes to its ground-state PES but at an elevated phonon state (Fig. 4a). As a result, the energy of the emitted photon is Stokes-shifted from the zero-phonon line, forming phonon replicas spaced by the phonon energy. In Fig. 4a, the emission lines are labelled with the corresponding phonon number state $|n\rangle$ in the ground-state PES. According to the Huang–Rhys theory for discrete phonon lines, the intensity of the *n*th phonon line is proportional to the overlap integral between the initial and final phonon states, that is, $|\langle 0, |, n\rangle|^2 = e^{-S}S^n/n!$, where *S* is the dimensionless Huang–Rhys factor measuring the strength of the exciton–phonon coupling. Therefore, the phonon line intensities have a Poisson distribution with an expectation value of *S*, as illustrated in Fig. 4a. In many other solid-state QEs, such as the colour centres in diamond, the coupling of defect emitters to bulk phonons produces phonon sidebands that are not well resolved due to the continuous phonon density of states in energy. In contrast, in Fig. 3a,b, we observe clearly resolved phonon lines generated by a single localized phonon mode that couples with a single IX in the QE.

The energy spacing of the phonon lines in the range of 3.0–5.0 meV matches the energy of the BM phonons in bilayer WSe_2. Time-resolved transmission measurements in pristine bilayer WSe_2 give the frequency and the coherence time of the BM phonon as 0.8 THz (or 3.4 meV) and 3.5 ps, respectively[21]. However, the interaction between the WSe_2 and the encapsulating hBN can cause mode hybridization that modulates the frequency of the BM phonon[47]. Additionally, the strong local strain gradient and the quantum confinement also affect the BM phonon frequency. As a result, we observe a spread of phonon line spacing in energy in the many devices we measured (see Supplementary Table 3 for a comprehensive dataset).

Fig. 4b shows the PL spectra of QE1 with increasingly negative gate voltage and a fixed pump power of 15 μW. In addition to a consistent redshift of the phonon lines, their intensity distributions change substantially, indicating the modulation of the phonon coupling strength *S*. We extract the *S* factors by fitting the peak intensities with the Poisson distribution[20]. Because the PES of the QEs is more complicated than the simple harmonic oscillator model assumed in the Huang–Rhys theory, the fitting has a large error, which outweighs the signal's noise, so it can only estimate the *S* factors. More details of the fitting method can be found in Supplementary Note 8. Despite the relatively large fitting errors, the result of *S* versus gate voltage in Fig. 3c clearly shows that *S* initially increases with the gate voltage, reaching a maximal value of 6.3 at ~−5V, and saturates thereafter. Although the coupling strength g_0 is proportional to the effective field across the materials, the dependence of *S* on the field is indirect and cannot be ascribed to a simple linear dependence. In particular, when the phonon coupling is large, the dependence of *S* on the coupling strength and electric field will involve the detailed change of the PES in response to the electric field. The saturation is possibly due to gate leakage and charge screening, which prevent further increase of the electric field, as also observable in the emission energy tuning in Fig. 3e. For comparison, we also measured *S* with increasing pump power and a fixed gate voltage of −6.4 V. *S* for the most part is unaffected by the pump

power. Our results show that the coupling between the colocalized quantum phonon mode and a single exciton can be precisely tuned by an electric field to a large value.

The colocalization of the IX and the BM phonon in the strain-engineered QE results in a very large coupling between them. The single exciton–phonon coupling can be described with the spin–boson interaction Hamiltonian: $H_{\mathrm{int},v} = g_0\sigma_z(b^\dagger + b)$, where b ($b^\dagger$) is the phonon annihilation (creation) operator on phonon number states $|n\rangle$, σ_z is the Pauli matrix on the basis of the ground ($|g\rangle$) and excited ($|e\rangle$) states of the exciton, and g_0 is the single exciton–phonon coupling rate[1,48]. The BM phonon directly modulates the dipole moment of the IX by adjusting the interlayer distance. Under an electric field E, the single-phonon–IX coupling rate[1] can be calculated from the zero-point amplitude ($\bar{x}_{\mathrm{zpf}}$) of the Γ-point BM: $g_0 = g^0 + 2eE\bar{x}_{\mathrm{zpf}}$, where $\bar{x}_{\mathrm{zpf}}$ is calculated from first-principles theory to be ~0.026 Å. g^0 is the zero-field coupling rate, which is calculated to be <0.08 meV, one order of magnitude smaller than the second term when the field is strong. Thus, assuming that the applied field can reach a reasonably high value of 0.25 V nm^{-1} in our device[49], g_0 can be increased to 1.3 meV. The system thus can reach the strong-coupling regime, satisfying $2g_0 > (\gamma_e, \gamma_p)$, where $\gamma_e \approx 1.17$ meV is the exciton linewidth (Fig. 2b) and $\gamma_p < 1.18$ meV is the BM phonon decoherence rate given its coherence time of 3.5 ps measured at room temperature[21]. At cryogenic temperatures and with better sample quality, we expect γ_e and γ_p can be further reduced.

Conclusions

We have created highly tunable QEs in WSe_2 bilayers by strain-engineering methods. An immediate next step is to integrate these emitters with integrated photonic platforms such as waveguides and photonic crystal cavities to achieve super-radiant emission, Purcell enhancement and cavity quantum electrodynamics. With twisted bilayer WSe_2 rather than a natural bilayer, the IX energy can be tuned electrically while still maintaining the characteristic valley states similar to those reported in moiré systems[28,29,50]. Furthermore, the demonstrated tunable phonon–photon coupling strength in these 2D QEs provides a new way to explore the quantum optomechanical effects. In many ways, the 2D QEs are analogous to cavity optomechanical systems, but at the atomic interface and with a phonon frequency of 0.8–1.0 THz, which is already at the ground state at the measurement temperature of 10 K. It will be possible to use a terahertz source to resonantly excite the phonon and prepare phonon Fock states in such a solid-state system at temperatures that are among the highest reported. The archetypical excitonic–optomechanical system demonstrated here thus has the potential to be a new quantum light resource that is entangled with single phonons[2,4] for use in quantum information processing, storage and communication[1,51–53].

Online content

Any methods, additional references, Nature Portfolio reporting summaries, source data, extended data, supplementary information, acknowledgements, peer review information; details of author contributions and competing interests; and statements of data and code availability are available at https://doi.org/10.1038/s41565-023-01410-6.

References

1. Aspelmeyer, M., Kippenberg, T. J. & Marquardt, F. Cavity optomechanics. *Rev. Mod. Phys.* **86**, 1391–1452 (2014).
2. Lee, K. C. et al. Entangling macroscopic diamonds at room temperature. *Science* **334**, 1253–1256 (2011).
3. Vivoli, V. C., Barnea, T., Galland, C. & Sangouard, N. Proposal for an optomechanical Bell test. *Phys. Rev. Lett.* **116**, 070405 (2016).
4. Tarrago Velez, S., Sudhir, V., Sangouard, N. & Galland, C. Bell correlations between light and vibration at ambient conditions. *Sci. Adv.* **6**, eabb0260 (2020).
5. Mirhosseini, M., Sipahigil, A., Kalaee, M. & Painter, O. Superconducting qubit to optical photon transduction. *Nature* **588**, 599–603 (2020).
6. Bienfait, A. et al. Phonon-mediated quantum state transfer and remote qubit entanglement. *Science* **364**, 368–371 (2019).
7. Toninelli, C. et al. Single organic molecules for photonic quantum technologies. *Nat. Mater.* **20**, 1615–1628 (2021).
8. Chen, W. et al. Continuous-wave frequency upconversion with a molecular optomechanical nanocavity. *Science* **374**, 1264–1267 (2021).
9. Aharonovich, I. & Toth, M. Quantum emitters in two dimensions. *Science* **358**, 170–171 (2017).
10. Lee, C. et al. Anomalous lattice vibrations of single- and few-layer MoS_2. *ACS Nano* **4**, 2695–2700 (2010).
11. Zhao, Y. et al. Interlayer breathing and shear modes in few-trilayer MoS_2 and WSe_2. *Nano Lett.* **13**, 1007–1015 (2013).
12. Palacios-Berraquero, C. et al. Large-scale quantum-emitter arrays in atomically thin semiconductors. *Nat. Commun.* **8**, 15093 (2017).
13. Branny, A., Kumar, S., Proux, R. & Gerardot, B. D. Deterministic strain-induced arrays of quantum emitters in a two-dimensional semiconductor. *Nat. Commun.* **8**, 15053 (2017).
14. Parto, K., Azzam, S. I., Banerjee, K. & Moody, G. Defect and strain engineering of monolayer WSe_2 enables site-controlled single-photon emission up to 150 K. *Nat. Commun.* **12**, 3585 (2021).
15. Peyskens, F., Chakraborty, C., Muneeb, M., Van Thourhout, D. & Englund, D. Integration of single photon emitters in 2D layered materials with a silicon nitride photonic chip. *Nat. Commun.* **10**, 4435 (2019).
16. Sortino, L. et al. Bright single photon emitters with enhanced quantum efficiency in a two-dimensional semiconductor coupled with dielectric nano-antennas. *Nat. Commun.* **12**, 6063 (2021).
17. Kundrotas, J. et al. Impurity-induced Huang–Rhys factor in beryllium δ-doped GaAs/AlAs multiple quantum wells: fractional-dimensional space approach. *Semicond. Sci. Technol.* **22**, 1070–1076 (2007).
18. Grosso, G. et al. Low-temperature electron–phonon interaction of quantum emitters in hexagonal boron nitride. *ACS Photonics* **7**, 1410–1417 (2020).
19. Li, D. et al. Exciton–phonon coupling strength in single-layer $MoSe_2$ at room temperature. *Nat. Commun.* **12**, 954 (2021).
20. Ergeçen, E. et al. Magnetically brightened dark electron–phonon bound states in a van der Waals antiferromagnet. *Nat. Commun.* **13**, 98 (2022).
21. Jeong, T. Y. et al. Coherent lattice vibrations in mono- and few-layer WSe_2. *ACS Nano* **10**, 5560–5566 (2016).
22. Altaiary, M. M. et al. Electrically switchable intervalley excitons with strong two-phonon scattering in bilayer WSe_2. *Nano Lett.* **22**, 1829–1835 (2022).
23. Darlington, T. P. et al. Imaging strain-localized excitons in nanoscale bubbles of monolayer WSe_2 at room temperature. *Nat. Nanotechnol.* **15**, 854–860 (2020).
24. Linhart, L. et al. Localized intervalley defect excitons as single-photon emitters in WSe_2. *Phys. Rev. Lett.* **123**, 146401 (2019).
25. Wang, Z., Chiu, Y. H., Honz, K., Mak, K. F. & Shan, J. Electrical tuning of interlayer exciton gases in WSe_2 bilayers. *Nano Lett.* https://doi.org/10.1021/acs.nanolett.7b03667 (2018).
26. Luo, Y., Liu, N., Kim, B., Hone, J. & Strauf, S. Exciton dipole orientation of strain-induced quantum emitters in WSe_2. *Nano Lett.* **20**, 5119–5126 (2020).
27. Huang, Z. et al. Spatially indirect intervalley excitons in bilayer WSe_2. *Phys. Rev. B* **105**, L041409 (2022).
28. Scuri, G. et al. Electrically tunable valley dynamics in twisted WSe_2/WSe_2 bilayers. *Phys. Rev. Lett.* **124**, 217403 (2020).
29. Tang, Y. et al. Tuning layer-hybridized moiré excitons by the quantum-confined Stark effect. *Nat. Nanotechnol.* **16**, 52–57 (2021).

30. Desai, S. B. et al. Strain-induced indirect to direct bandgap transition in multilayer WSe_2. *Nano Lett.* **14**, 4592–4597 (2014).
31. Jin, C. et al. Interlayer electron–phonon coupling in WSe_2/hBN heterostructures. *Nat. Phys.* **13**, 127–131 (2017).
32. Li, Z. et al. Emerging photoluminescence from the dark-exciton phonon replica in monolayer WSe_2. *Nat. Commun.* **10**, 2469 (2019).
33. Paradisanos, I. et al. Efficient phonon cascades in WSe_2 monolayers. *Nat. Commun.* **12**, 538 (2021).
34. Rivera, P. et al. Intrinsic donor-bound excitons in ultraclean monolayer semiconductors. *Nat. Commun.* **12**, 871 (2021).
35. Jones, A. M. et al. Spin-layer locking effects in optical orientation of exciton spin in bilayer WSe_2. *Nat. Phys.* https://doi.org/10.1038/nphys2848 (2014).
36. Kumar, S., Kaczmarczyk, A. & Gerardot, B. D. Strain-induced spatial and spectral isolation of quantum emitters in mono- and bilayer WSe_2. *Nano Lett.* **15**, 7567–7573 (2015).
37. Lindlau, J. et al. The role of momentum-dark excitons in the elementary optical response of bilayer WSe_2. *Nat. Commun.* https://doi.org/10.1038/s41467-018-04877-3 (2018).
38. Aslan, B., Deng, M., Brongersma, M. L. & Heinz, T. F. Strained bilayer WSe_2 with reduced exciton–phonon coupling. *Phys. Rev. B* **101**, 15305 (2020).
39. Baek, H. et al. Highly energy-tunable quantum light from moiré-trapped excitons. *Sci. Adv.* **6**, eaba8526 (2020).
40. Liu, Y. et al. Electrically controllable router of interlayer excitons. *Sci. Adv.* https://doi.org/10.1126/sciadv.aba1830 (2020).
41. Zhang, S. et al. Defect structure of localized excitons in a WSe_2 monolayer. *Phys. Rev. Lett.* **119**, 046101 (2017).
42. Rhodes, D., Chae, S. H., Ribeiro-Palau, R. & Hone, J. Disorder in van der Waals heterostructures of 2D materials. *Nat. Mater.* **18**, 541–549 (2019).
43. Zheng, Y. J. et al. Point defects and localized excitons in 2D WSe_2. *ACS Nano* **13**, 6050–6059 (2019).
44. Tsai, J.-Y., Pan, J., Lin, H., Bansil, A. & Yan, Q. Antisite defect qubits in monolayer transition metal dichalcogenides. *Nat. Commun.* **13**, 492 (2022).
45. Lu, X. et al. Optical initialization of a single spin-valley in charged WSe_2 quantum dots. *Nat. Nanotechnol.* **14**, 426–431 (2019).
46. Barati, F. et al. Vibronic exciton–phonon states in stack-engineered van der Waals heterojunction photodiodes. *Nano Lett.* **22**, 5751–5758 (2022).
47. Grzeszczyk, M. et al. Breathing modes in few-layer $MoTe_2$ activated by h-BN encapsulation. *Appl. Phys. Lett.* **116**, 191601 (2020).
48. Yeo, I. et al. Strain-mediated coupling in a quantum dot–mechanical oscillator hybrid system. *Nat. Nanotechnol.* **9**, 106–110 (2014).
49. Unuchek, D. et al. Valley-polarized exciton currents in a van der Waals heterostructure. *Nat. Nanotechnol.* **14**, 1104–1109 https://doi.org/10.1038/s41565-019-0559-y (2019).
50. Devakul, T., Crépel, V., Zhang, Y. & Fu, L. Magic in twisted transition metal dichalcogenide bilayers. *Nat. Commun.* **12**, 6730 (2021).
51. Galland, C., Sangouard, N., Piro, N., Gisin, N. & Kippenberg, T. J. Heralded single-phonon preparation, storage, and readout in cavity optomechanics. *Phys. Rev. Lett.* **112**, 143602 (2014).
52. Anderson, M. D. et al. Two-color pump–probe measurement of photonic quantum correlations mediated by a single phonon. *Phys. Rev. Lett.* **120**, 233601 (2018).
53. Barzanjeh, S. et al. Optomechanics for quantum technologies. *Nat. Phys.* **18**, 15–24 (2021).

Methods

Device fabrication

A 17 × 17 array of nanopillars, each with a diameter of 140 nm, a height of 200 nm and spaced with a 2.5 μm pitch, were patterned on 300 nm SiO_2 deposited by electron-beam evaporation using electron-beam lithography. The 2D material heterostructure consists of bilayer WSe_2 encapsulated by hBN around 30 nm thick with few-layer graphite as top- and bottom-gate electrodes. In some devices, an additional graphite layer is transferred in contact with the WSe_2 to control the doping of the material. The heterostructure is stacked and transferred onto the nanopillar array by a conventional dry transfer method using polycarbonate/polydimethylsiloxane (Sylgard 184) stamps. After the device has been transferred, contact electrodes of Ti/Au to the graphite were patterned with photolithography using a direct laser writer and deposition using electron-beam evaporation. An optical image of a device is shown in Fig. 1d, where the strain induced by the nanopillars is visible.

PL measurement method

The sample was wire bonded to a sample holder and loaded into a cryostat (Montana Cyrostation S-100) to be cooled to 10 K for measurement. A leakage test was done to ensure that the electrodes are not shorted together, and then the PL spectra of strained heterostructure can be measured at different bias voltages. A continuous-wave helium–neon laser (632.8 nm) was used to excite the excitons. The laser beam was focused on the sample through an optical window in the cryostat with a 50× objective lens (numerical aperture, 0.42) to achieve a diffraction-limited spot size of about 1 μm in diameter. The IX emission was passed through a 633 nm notch filter to remove the reflected signal of the laser before being acquired with a spectrometer (Princeton Instruments, IsoPlane 320).

Measurement of $g^{(2)}(0)$

Using the same set-up as above, after filtering the laser light with the 633 nm notch filter, the emission signal was then filtered with a tunable distributed Bragg reflector filter with 4 nm bandwidth (810 nm at an incident angle of 0°, and 800 nm at 19°) to select a single emitter line. The signal was then split with a beam splitter and sent to two single-photon detectors (Excelitas, SPCM-AQRH-16) which fed into a time-to-digital converter (ID Quantique) for the time-tagged time-resolved data acquisition.

First-principles calculations

DFT calculations were performed using the Quantum Espresso[54] package. The Perdew–Burke–Ernzerhof functional[55] and optimized norm-conserving Vanderbilt pseudopotential[56] were used. The dispersion correction with the D2 form was used to consider the van der Waals interaction[57]. The optimized lattice constant and interlayer distance are 3.334 Å and 6.417 Å, respectively. The phonon dispersion and vibration mode were calculated based on density functional perturbation theory. The zero-point amplitude for the BM was calculated as the average of the mean square displacement at the zero temperature, that is, $\bar{x}_{\mathrm{zpf}} = \frac{1}{6}\sum_i \sqrt{\frac{\hbar}{2M_i\omega}}|\xi_i|$, where ξ_i is the eigenvector, M_i is the mass of the ith atom in the unit cell and ω is the phonon frequency.

Data availability

The data that support the findings of this study are available from the corresponding author upon reasonable request.

References

54. Giannozzi, P. et al. Quantum Espresso: a modular and open-source software project for quantum simulations of materials. *J. Phys. Condens. Matter* **21**, 395502 (2009).
55. Perdew, J. P., Burke, K. & Ernzerhof, M. Generalized gradient approximation made simple. *Phys. Rev. Lett.* **77**, 3865–3868 (1996).
56. Hamann, D. R. Optimized norm-conserving Vanderbilt pseudopotentials. *Phys. Rev. B* **88**, 085117 (2013).
57. Grimme, S. Semiempirical GGA-type density functional constructed with a long-range dispersion correction. *J. Comput. Chem.* **27**, 1787–1799 (2006).

Acknowledgements

This work was supported by the National Science Foundation (NSF award number EFMA 1741656, ECCS-2006103, and NSF DMR-1719797). Part of this work was conducted at the Washington Nanofabrication Facility/Molecular Analysis Facility, a National Nanotechnology Coordinated Infrastructure (NNCI) site at the University of Washington with partial support from the NSF via awards NNCI-1542101 and NNCI-2025489. A.R. received funding from NSF award DGE-2140004.

Author contributions

A.R., R.P. and M.L. conceived the research. A.R. and R.P. fabricated the devices and performed the measurements. X.Z. and T.C. performed the theoretical analysis. S.C., K.F., M.H. and X.X. assisted with single-photon autocorrelation measurements. A.R. analysed the data. A.R., R.P., T.C. and M.L. co-wrote the paper with contributions from all authors.

Competing interests

The authors declare no competing interests.

Additional information

Supplementary information The online version contains supplementary material available at https://doi.org/10.1038/s41565-023-01410-6.

Correspondence and requests for materials should be addressed to Ruoming Peng or Mo Li.

Peer review information *Nature Nanotechnology* thanks Donghai Li and the other, anonymous, reviewer(s) for their contribution to the peer review of this work.